Experimental study of a Francis turbine under variable-speed and discharge conditions

Chirag Trivedi[1]

Researcher, Waterpower Laboratory, Department of Energy and Process Engineering, Norwegian University of Science and Technology, Norway.

Einar Agnalt

Ph. D. Candidate, Waterpower Laboratory, Department of Energy and Process Engineering, Norwegian University of Science and Technology, Norway.

Ole Gunnar Dahlhaug

Professor, Waterpower Laboratory, Department of Energy and Process Engineering, Norwegian University of Science and Technology, Norway.

ABSTRACT

This work investigates the unsteady pressure fluctuations in a hydraulic turbine that are observed during steep ramping. Although hydraulic turbines are expected to operate seamlessly during steep ramping, the resulting pressure amplitudes are so significant that they take a toll on a machine's operating life. Objective of the present study is to investigate time-dependent pressure amplitudes in the vaneless space, runner and draft tube during power ramping-up and -down under variable-speed configuration. Novelty is to vary both discharge and rotational speed of a runner. The measurements are performed on a high-head model Francis turbine. The investigations revealed that amplitudes of characteristics frequencies, especially rotor-stator interaction, are small during steep ramping however, at the end of transient cycle, the amplitudes quickly increased 30-fold. During steep ramping, blade passing frequency was appeared in the runner, which is uncommon phenomenon in high-head Francis turbines. Strong reflection of pressure waves towards runner from vaneless space (guide vane walls) may be one of the causes for the appearance of blade passing frequency in the runner.

Keywords: hydropower; turbine; electricity; pressure; load variation; variable-speed.

1. Introduction

Electricity is produced using both continual and intermittent types of energy sources. Competitive electricity prices and the inclination towards wind and solar energy have forced industries to utilize

[1]Corresponding author. Postal address: Vannkraftlaboratoriet, Alfred Getz vei. 4, NTNU, NO-7491 Trondheim, Norway. Tel: +47 735 93849. E-mail: chirag.trivedi@ntnu.no

intermittent energy sources. This has resulted in power imbalance and frequent grid disruptions [1]. For the stable and uninterrupted operation of a power grid, demand factor (i.e. electricity demand/generation) must be maintained within the allowable limit [2]. Hydropower is considered as a vital alternative to accommodate the real-time demand after the gas turbine. The gas turbines have generally low efficiency and the cost per kWh is more than the hydropower. The large-scale power plants such as thermal, nuclear and geothermal are operated at their maximum efficiency point, and the response time is very low.

Hydraulic turbines have capability to change power output by 1-25 MW per second, depending upon turbine type and the power generation capacity [3,4]. Output power is regulated using one of three approaches: (1) low flexibility- Synchronous speed and constant discharge, (2) medium flexibility- synchronous speed and variable discharge and (3) high flexibility- variable speed and discharge. The first approach is used for run of river power plant where guide vanes are fixed permanently (or no guide vanes) to reduce the operating/maintenance cost. Turbines are operated for the fixed load depending on available head/discharge and are not applicable to meet the real-time demand. The second approach is widely used due to high efficiency and low cost. Turbines are operated at the best efficiency point (BEP) except load picking hours. Such turbines experience dynamic instability when they are operated at the off-design load, i.e. away from BEP [5–7]. Third approach provides moderate to high flexibility to meet real-time demand and stabilize the power grid when wind/solar power fluctuates rapidly [8,9]. Advantage of this approach is the flexibility of two variables, i.e. angular speed and discharge, which enables the wide range of power output and two different combinations for the same load. Thus, dynamic stability can be maintained unlike the second approach.

Currently, research is inclined towards design and development of a variable-speed turbine [2], that will accommodate increased numbers of transients cycles, i.e. start-stop/load-variation. Traditionally, turbines are designed for certain numbers of transient cycles during their operating life [10] and majority of them exceed the limit within half of their life [11,12]. Each transient cycle costs runner life equivalent to certain numbers of operating hours [13–19]. Moreover, turbine operating cost increases with the

number of transient cycles and it becomes unprofitable to operate a turbine due to low electricity prices when wind/solar power is high. Further, when the demand is low, turbines are operated at off-design load, which causes more fatigue to the turbine (thus high operating cost) as compare to the profit margin [20–22]. The developed fatigue loading is directly associated with the unsteady pressure pulsations in the turbine [23–25].

During the transient cycle, pressure loading is not coherent as observed for steady operating conditions. The pressure amplitudes vary rapidly during load change [26,27]. Experimental studies (using second approach) on a Francis turbine showed that the pressure amplitudes during the transient cycles can vary up to three times that of the steady BEP load in short time span [28–33] depending upon the rate of guide vane movement and the runner angular speed. In a high head turbine, vaneless space (a space between runner and guide vanes) is very small [34] and the amplitudes of rotor-stator-interaction (RSI) frequencies are high. This results in time dependent stresses in the blades [35]. In addition, development of swirl in the blade passages due to guide vane movement causes flow separation and asymmetric blade loading [36]. The rate of guide vane movement is defined by considering the exterior parameters such as water hammer, surging, runner inertia and the runner torque [37]. For more reliable design of a runner, unsteady pressure loading on the blades with respect to guide vane aperture is equally important [38].

Very few numerical studies have been performed to investigate the transient operating conditions of hydraulic turbines [39]. One the key challenges is requirement of computational power to perform simulations with guide vane opening/closing, i.e., mesh deformation. To save simulation time and resources, blade and guide vane passages are modelled and good agreement between the experimental and numerical pressure loading was obtained [40–42]. The numerical results enabled to estimate the fatigue loading on the blades. However, this approach requires two-way coupling and the simulation time is extremely long due to involved complexities of structural deformation [43–45]. A new approach of turbine simulation is considered in recent years that allows coupling between 1D and 3D simulations [46]. Simulation of conduit system including penstock is performed using 1D approach whereas

simulation of the turbine is performed using 3D approach. Thus, simulation time can be saved to a certain extent.

In order to cope with the variable electricity demand from end users and variable power generation from the wind/solar energy, research on variable-speed technology of hydraulic turbines is vital. Currently, it is a good alternative as it allows stable performance at off-design conditions and wide range of combinations. When both runner angular speed and discharge vary, complex pressure and velocity field is developed in the runner. Flow angle, tangential velocity and swirl component of velocity vary in time. Therefore, it is important to study how a pressure field changes for variable-speed configuration and how pressure amplitudes vary [47]. Current study focuses on: (1) how a pressure field varied with the discharge and runner angular speed, (2) what are the pressure amplitudes at different locations inside the turbine, (3) how torque/power changes, (4) what is the flow condition in the runner and draft tube when a turbine operates at the part-/minimum-load and (5) how flow condition changes when the load changes from a stable to the unstable condition, i.e. off-design.

2. Measurements

2.1 Test facility

The test rig available at the Waterpower laboratory of the Norwegian University of Science and Technology is used for the experimental studies. This test rig is capable of operating under two configurations (closed and open loop) according to measurements. The closed loop is preferred for steady-state measurement while the open loop is preferred for transient measurements because the open loop provides hydraulic system to the prototype. Figure 1 shows open loop hydraulic system. Water from a large reservoir (9) was continuously pumped to an overhead tank (2) then flowed down to the turbine (7). Discharge to the turbine was regulated by guide vanes. Feed pump (1) was operated at the selected speed to maintain constant head. Two pumps are driven by a 315 kW variable speed motor, and the pumps can be operated in series or parallel depending on discharge/head discharge/head requirements for the measurements. Draft tube outlet was connected to a suction tank (8) wherein a constant water level was maintained at atmospheric pressure, and water above the runner centerline was

discharged to the basement (9). The open loop can produce head up to 16 m whereas the closed loop can produce a head up to 100 m (discharge up to 0.5 $m^3 s^{-1}$). For our measurements, an open loop was used to enable variable-speed configurations similar to a prototype. The investigated Francis turbine was a reduced scale (1:5.1) model of a prototype operating at Tokke power plant in Norway. The turbine included 14 stay vanes integrated within spiral casing, 28 guide vanes, a runner with 15 blades and 15 splitters, and a draft tube. The runner inlet and outlet diameters are 0.63 m and 0.347 m, respectively. Estimated Reynolds numbers are 1.87×10^6 at the runner outlet for the BEP.

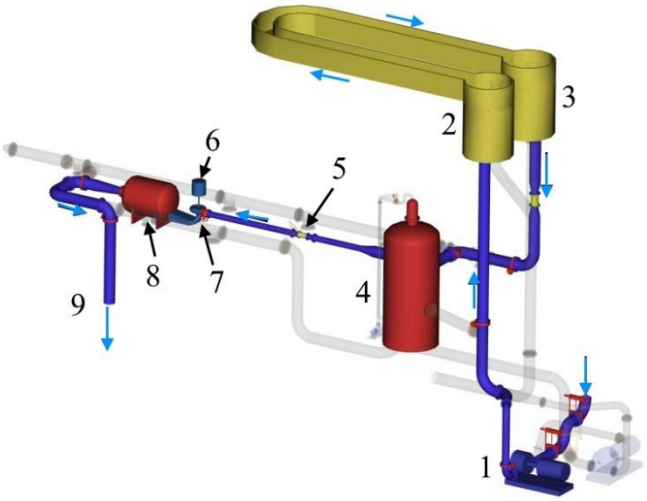

Figure 1 Open loop hydraulic system at the Waterpower laboratory, NTNU. (1) feed pump (2) overhead tank-primary, (3) overhead tank-secondary, (4) pressure tank, (5) magnetic flowmeter, (6) induction generator, (7) Francis turbine, (8) suction tank and (9) basement.

The turbine runner and generator rotor were mounted on the same shaft therefore, runner angular speed was proportional to the rotor speed. For the variable-speed measurements, a developed LabView program was integrated with the governing system that allowed to regulate both guide vane movement and frequency controller at same time. However, the actual variation may be dependent on the system inertia, water mass acting on the guide vanes and the response time. Frequency response time was much higher than the data logging rate. Therefore, delay in data digitization was almost null as compared to the time-scale of load change.

2.2 Instrumentation and calibration

The Francis turbine was equipped with all instruments required to carry out model testing according to IEC 60193 [48]. Additional pressure sensors were mounted at different locations in the turbine.

Figure 2 shows the locations of the pressure sensors in the turbine. Two sensors (VL1 and VL2) are in the vaneless space to acquire RSI frequencies and amplitudes; four sensors (R1, R2, R3 and R4) are on the runner crown, between two blades; four sensors (DT1, DT2, DT3, and DT4) are on the wall of the draft tube cone to investigate the vortex breakdown from the runner outlet. Two sensors (IN1 and IN2) are mounted at the turbine inlet conduit to monitor the water hammer.

Calibration and uncertainty quantification of all measuring instruments and sensors were conducted. IEC 60193 was followed to quantify the uncertainties, which are shown in Table 1. The total uncertainty $(\delta_{\eta h})_{t,BEP}$ includes both systematic and random uncertainties (see Equation (2)). The systematic uncertainty is the square-sum-root of the discharge (δ_Q), head (δ_H), torque (δ_T) and runner angular speed (δ_n). Total uncertainty in the hydraulic efficiency ($\delta_{\eta ht}$) is ±0.2%, which includes a random uncertainty ($\delta_{\eta hr}$) of ±0.18% at BEP. The uncertainties of the pressure sensors located in the vaneless space, runner and draft tube are ±0.12, ±0.26 and ±0.14%, respectively. Further, discharge through the upper labyrinth seal was measured to estimate the volumetric efficiency of the turbine, and uncertainty of the seal discharge (δ_{q1}) measurement was ±0.26%. Uncertainty in guide vane angular positioning (δ_α) was measured as ±0.7%. A repeatability study was conducted at BEP and PL operating conditions to check any deviations over a certain period. The maximum deviation in the hydraulic efficiency at BEP and PL was less than ±0.05% and ±0.1%, respectively. Hence, random uncertainty is less than the total uncertainty.

$$\left(\delta_{\eta_h}\right)_s = \pm\sqrt{\left(\delta_Q\right)_s^2 + \left(\delta_H\right)_s^2 + \left(\delta_T\right)_s^2 + \left(\delta_n\right)_s^2 + \left(\delta_{\rho,\text{water}}\right)_s^2} \tag{1}$$

$$\left(\delta_{\eta_h}\right)_{t,\text{BEP}} = \pm\sqrt{\left(\delta_{\eta_h}\right)_s^2 + \left(\delta_{\eta_h}\right)_r^2} \tag{2}$$

Table 1 Computed uncertainties in the flow measurement. The uncertainties are in percentage of the measured value.

δ_H	δ_Q	δ_{q1}	δ_{p1}	δ_T	δ_n	$\delta_{\eta hr}$	$\delta_{\eta ht}$	δ_{VL}	δ_R	δ_{DT}	δ_α
±0.17	±0.12	±0.26	±0.023	±0.15	±0.035	±0.18	±0.2	±0.12	±0.26	±0.14	±0.7

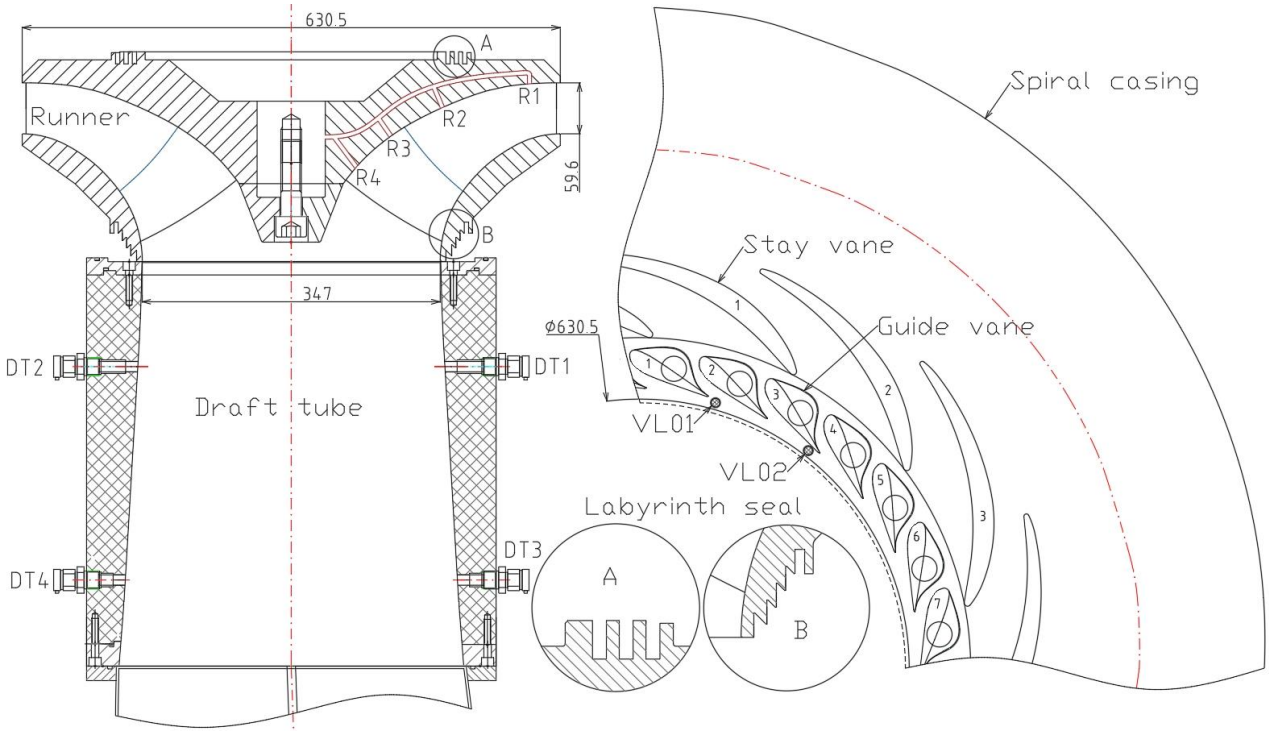

Figure 2 Locations of pressure sensors in the turbine. Sensors R1, R2, R3 and R4 are in the runner; DT1, DT2, DT3 and DT4 are in the draft tube cone; VL1 and VL2 are in the vaneless space.

2.3 Performance study

Experiments at the steady-state operating conditions were carried out before the transient. The results were compared with the benchmark data to confirm repeatability of the test-rig. The constant efficiency hill diagram is shown in Figure 3. The BEP is located at α=9.9°, n_{ED}=0.18 and Q_{ED}=0.15 where the hydraulic efficiency is 93.1±0.2%.

$$n_{ED} = \frac{nD}{\sqrt{E}} \quad (-) \tag{3}$$

$$Q_{ED} = \frac{Q}{D^2\sqrt{E}} \quad (-) \tag{4}$$

Table 2 summarizes the flow parameters at BEP, PL and FL used for the current study. The runner synchronous speed was 5.5 Hz. Total 10 repetitions were made for each condition and the deviation was within the uncertainty. The repetition study showed no shift from the trend line. This has confirmed that both turbine and test rig perform well under steady conditions and can be used for transient measurements.

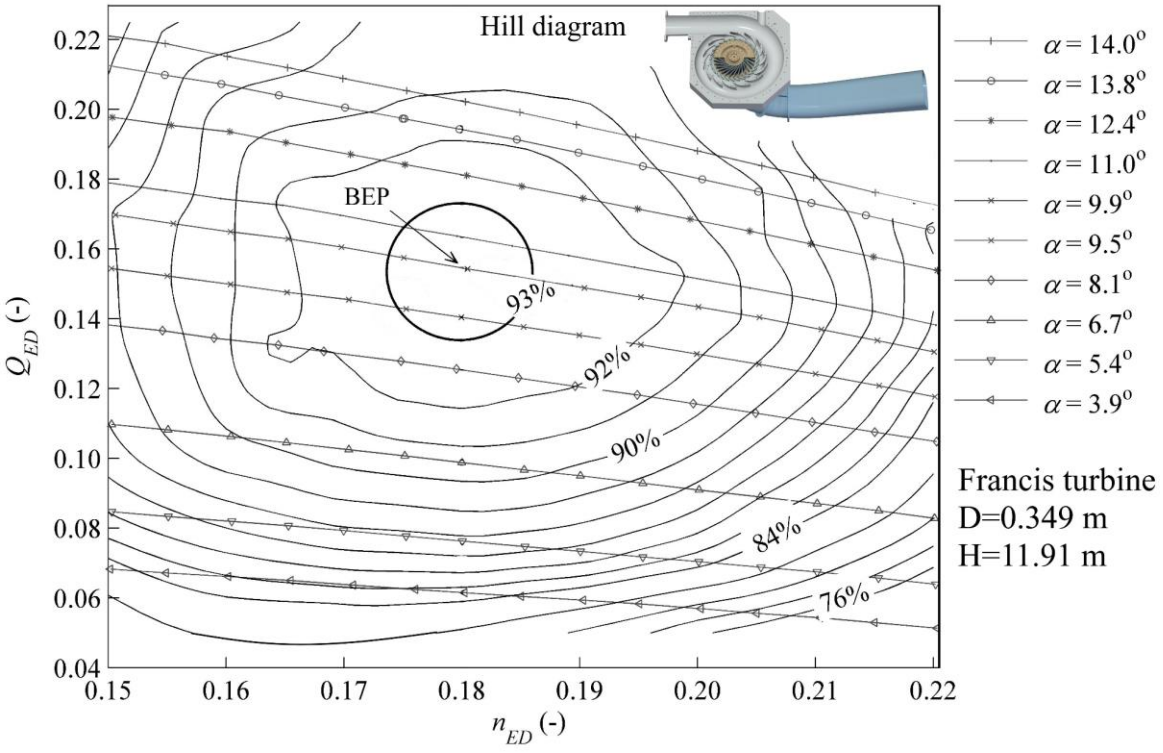

Figure 3 Constant efficiency hill diagram of the investigated model Francis turbine. Q_{ED} and n_{ED} are the dimensionless quantities of discharge and speed, respectively. n_{ED}=0.18 is the synchronous speed of the turbine.

Table 2 Summary of the parameters observed at the steady-state operating conditions of the turbine.

OP	***α* (°, %)**	***Q* ($m^3 s^{-1}$)**	***H* (m)**	***T* (Nm)**	***n* (Hz)**	***η*$_h$ (%)**	***Q*$_{ED}$ (-)**	***n*$_{ED}$ (-)**
PL	7, 65	0.131	12.14	337.9	5.5	91.2	0.09	0.18
BEP	10, 100	0.199	11.94	620.7	5.5	93.1	0.15	0.18
FL	14, 140	0.263	11.64	781.9	5.5	92.1	0.20	0.18

Transient characteristics of the turbine:

- For constant guide vane aperture: discharge is inversely proportional to the runner angular speed.
- For constant speed: torque is directly proportional to the discharge (guide vane aperture).

2.4 Range of parameters

Current study focuses on the unsteady pressure measurements for variable-speed configurations. Runner angular speed and guide vane angle were changed from the corresponding steady load. Steady state PL, BEP and HL were considered as initial points for the load variation. For example, to reduce the load (ramp-down) by 30% from BEP, guide vanes were closed from 10° to 7° linearly. At same time, runner angular speed was reduced from 5.5 Hz to 3.9 Hz. Measurements were conducted for total

six configurations of load variation and the dimensionless parameters at the start and end of load variation are shown in the Table 3.

- load variation from BEP (100% load) and reverse,
- load variation from PL (65% load) and reverse,
- load variation from FL (140% load) and reverse.

Table 3 Dimensionless parameters, speed factor (n_{ED}) and discharge factor (Q_{ED}), at the start and end of load variation.

OP	**BEP**		**PL**		**FL**	
Transient	Start	End	Start	End	Start	End
n_{ED}	0.18	0.124	0.18	0.125	0.18	0.127
Q_{ED}	0.15	0.124	0.099	0.072	0.203	0.18

Experimental data were analyzed for all configurations. Trend and relative variation of the global parameters such as head, discharge, torque, power and efficiency during load change is similar for all cases. Therefore, these parameters are elaborated for one transient condition. For the unsteady pressure loading, trend is nearly similar for all transient cases except pressure amplitudes. At BEP, amplitudes of RSI frequencies are small. At PL, the amplitudes are large and additional frequency of vortex breakdown is obtained.

During the measurements, available pressure in the draft tube was above the atmospheric pressure and water temperature was 15 °C. Therefore, cavitation was not occurred in the test rig and the measurements correspond to cavitation free conditions.

3. Analysis of transient results

3.1 Load reduction (ramp-down)

Figure 4 shows change of guide vane aperture, runner angular speed, torque, power output and net head during load reduction from BEP. The parameters are normalized using steady-state values at BEP, and the load reduction begins at 0 s.

$$x^* = \frac{x}{x_{BEP}} \quad (-) \tag{5}$$

Turbine was operating at steady BEP load where the guide vane aperture was 100%, and the runner was spinning at 5.5 Hz. To reduce the load, the guide vanes were closed linearly at the rate of 0.6° per second. Similarly, runner angular speed was decreased linearly from 5.5 to 3.9 Hz. Approximately 30% load was reduced in 5 s. Overshoot of head value at t=5 s was seen due to rapid closing of the guide vanes. For variable-speed configurations, power ramp-up and ramp-down time is important to balance the power grid parameters and/or to maintain the power quality. That is dependent on (1) how quickly runner angular speed is changed, (2) inertia of rotating system (flywheel effect) including water mass and (3) energy transferred by the blades. Rapid movement of the guide vanes is avoided due to the risk of water hammer. Changing runner angular speed may be viable option to meet the instantaneous electricity demand. However, the instantaneous change is dependent on the stored energy and the system inertia. In this turbine, as seen in Figure 4, inertial effect is dominating from 0 s to 2 s, where the power output increases quickly. For a prototype, inertial effect is estimated at the time of commissioning using runner acceleration (ω), the polar moment of inertia of the rotating masses (J) and the torque (T).

$$t_{\text{start}} = \frac{J\omega}{T} \quad \text{(s)} \tag{6}$$

The mechanical start time is dependent on the flywheel effect (GD^2) of the rotating structure, runner acceleration (ω^2) and power (P),

$$t_m = \frac{GD^2\omega^2}{P} \quad \text{(s)} \tag{7}$$

In addition to the inertial effect, change of torque value can be explained using Euler equation and velocity triangles. Figure 5 shows a blade passage, a guide vane passage and velocity triangles at the runner inlet and outlet. Velocity triangles are shown for both conditions, i.e. BEP and after 30% load reduction. Whirl velocity (c_u), specific energy (e) torque (T), power (P) and efficiency can be estimated using following equations;

$$c_u = u - c_m \cot\beta, \tag{8}$$

$$e = c_{m1}^2 \cot\alpha_1 \left(\cot\alpha_1 + \cot\beta_1\right), \tag{9}$$

$$T = m\left(c_{u1}r_1 - c_{u2}r_2\right), \tag{10}$$

$$P = T\omega = m\left(c_{u1}u_1 - c_{u2}u_2\right), \tag{11}$$

$$\eta = \frac{c_{u1}u_1 - c_{u2}u_2}{gH}. \tag{12}$$

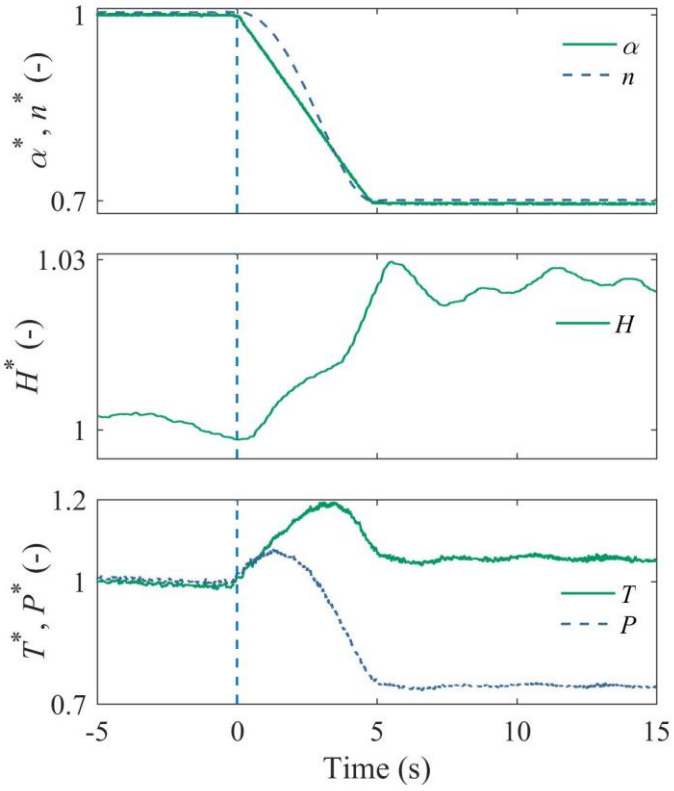

Figure 4 Change of guide vane angle (α), runner angular speed (n), torque (T), power output (P) and net head (H) during 30% load reduction from BEP. Time t=0 s corresponds to start time of load change.

In the investigated Francis runner, inlet and outlet blade angles are 57 and 15°, respectively. The runner inlet and outlet radius is 315 and 173.5 mm, respectively. Variation of whirl and tangential velocity at the runner inlet during load change is shown in Figure 6. Whirl (c_{u1}) and tangential (u_1) components are normalized by the corresponding velocity components at BEP, which are 9.85 and 11 m s^{-1}, respectively. Both components linearly follow the trend of guide vane movement (discharge) and the runner angular speed. Approximately 30 and 32% reduction in the whirl and tangential velocity can be seen.

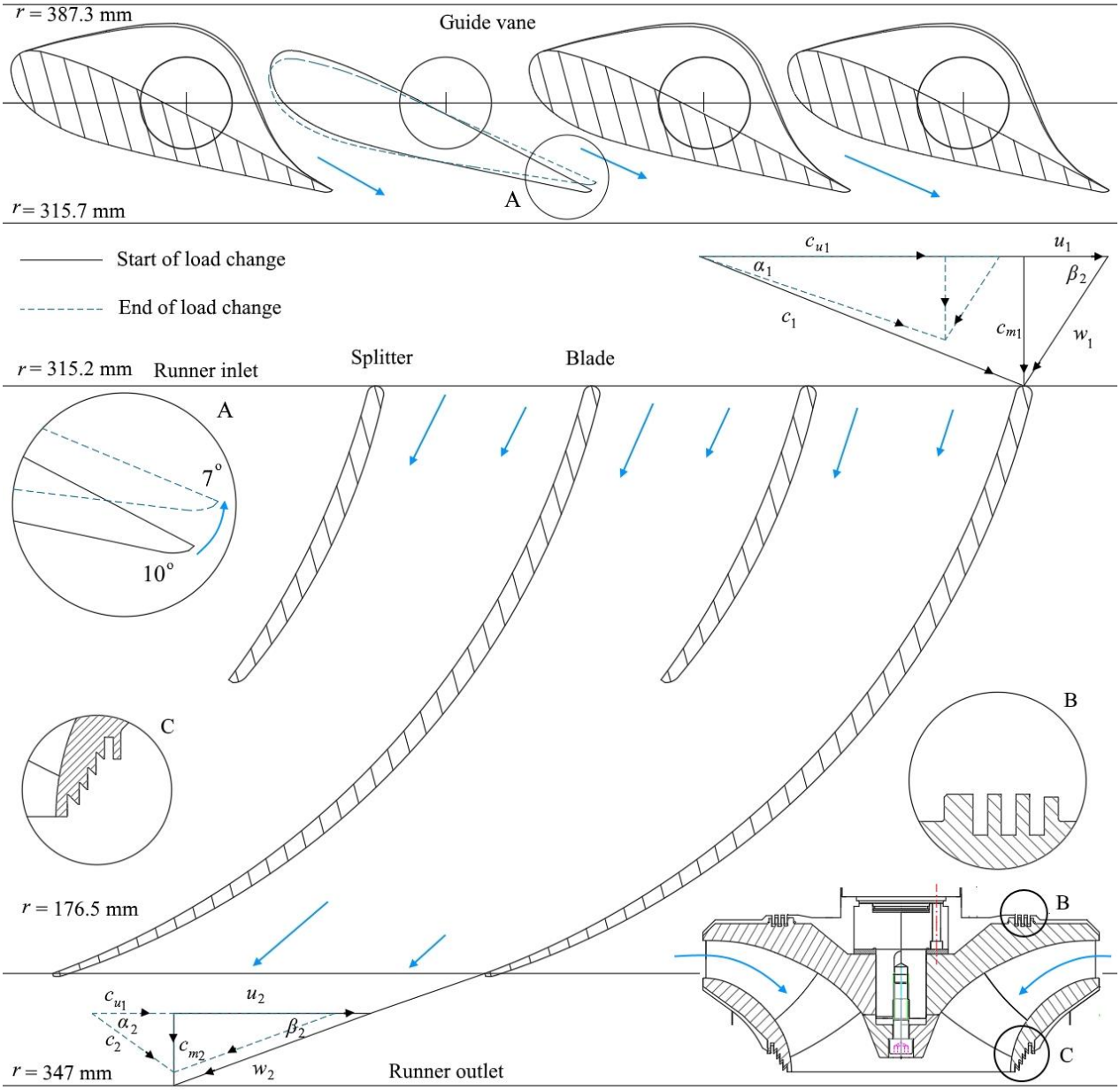

Figure 5 A blade passage, a guide vane passage and the velocity triangles at the runner inlet and outlet of the investigated Francis turbine. Continuous and dotted line velocity triangles correspond to the time before and after the load change, respectively. A-enlarged view of the guide vane movement, B-enlarged view of upper labyrinth seal and C-enlarged view of lower labyrinth seal.

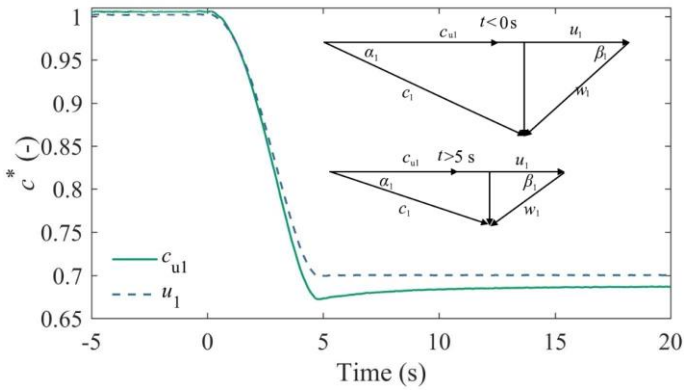

Figure 6 Whirl and tangential velocity components at the runner inlet during load reduction from BEP. Time *t*=0 s corresponds to start time of load change.

Ten pressure sensors were mounted at different locations in the turbine to investigate amplitudes of time-dependent pressure loading. Two additional pressure sensors were mounted at the inlet conduit to study water hammer during load change. Figure 7 shows time-average pressure during 30% load reduction from BEP. IN1 and IN2 are locations of flush mount sensors in the conduit (d=0.35 m), and their respective locations are 7.8 and 0.88 m from the turbine axis. Measurement uncertainty form the calibration of IN1 and IN2 sensors is ±0.07%. The pressure data are normalized using Equation (13), i.e. factor of pressure fluctuations,

$$\tilde{p}_{\mathrm{E}} = \frac{\tilde{p}(t)}{(\rho E)_{\mathrm{BEP}}}. \tag{13}$$

The head loss between IN1 and IN2 is 0.5% before the load change and is less than 0.1% after the load change. Effect of pressure surge at 4.8 s can be seen clearly, and the total head rise was 0.4 m during the transient period. Pressure oscillations are damped out at 15 s. Spectral analysis of the pressure data was carried out to study frequency content and amplitudes. Figure 7 (right) shows frequency spectrum and corresponding amplitudes ($\tilde{p}_{\mathrm{E\,RMS}}$) in time domain at IN2 location.

$$\tilde{p}_{\mathrm{E\,RMS}} = \frac{\tilde{p}(t) - p(t)_{\mathrm{RMS}}}{(\rho E)_{\mathrm{BEP}}} \tag{14}$$

Before the load change, turbine was operating at steady BEP load where the highest amplitudes are associated to the blade passing frequency (f_{b}) 167 Hz and its harmonic.

$$f_{\mathrm{b}} = nZ_{\mathrm{b}} \qquad (\mathrm{Hz}) \tag{15}$$

During 2-4 s, amplitudes of blade passing frequency are extremely small, which increases gradually after 4 s. Turbine inlet conduit was connected to the pressure tank which developed standing waves of different frequencies 15, 27 and 41 Hz depending upon the flow condition. Low-frequency pressure pulsations, 14.95 Hz, can be seen with high amplitudes, twice the amplitude of blade passing frequency.

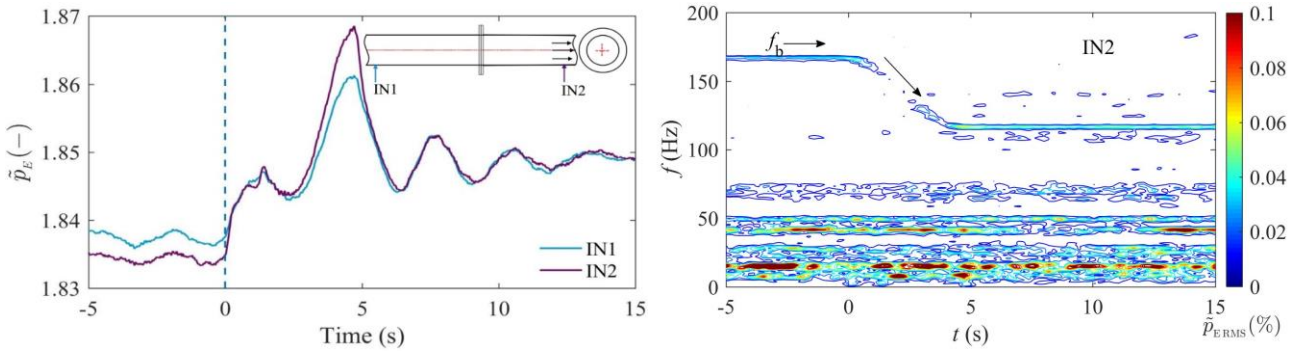

Figure 7 Time-average pressure variation and spectral analysis at the turbine inlet conduit during 30% load reduction from BEP. IN1 and IN2 are the locations of pressure measurement, 0 s corresponds to start time of load reduction.

For the current study, two pressure sensors VL1 and VL2 were mounted in the vaneless space; VL1 was located between two guide vanes, and VL2 was located at the trailing edge. Amplitudes of blade passing frequency at VL2 are 1.33 times that of VL1. Figure 8 (left) shows acquired pressure from VL2 location during load change, and Figure 8 (right) shows fluctuations from 4.88 s to 5 s at VL1 and VL2 locations. The amplitudes are within the limit of ±2σ, where σ is the time-average standard deviation. **Error! Reference source not found.**Time of 0.02 s corresponds to approximate 180° angular movement of the runner. The pressure pulsations correspond to the blade passing frequency. When a blade is front of the sensor, pressure pick is developed, marked as t_1 in the figure. When the sensor position is in the middle of the blade passage, pressure is low, marked as t_2. Thus, simultaneous interaction takes place as runner advances. Phase difference between VL1 and VL2 is 4.2°.

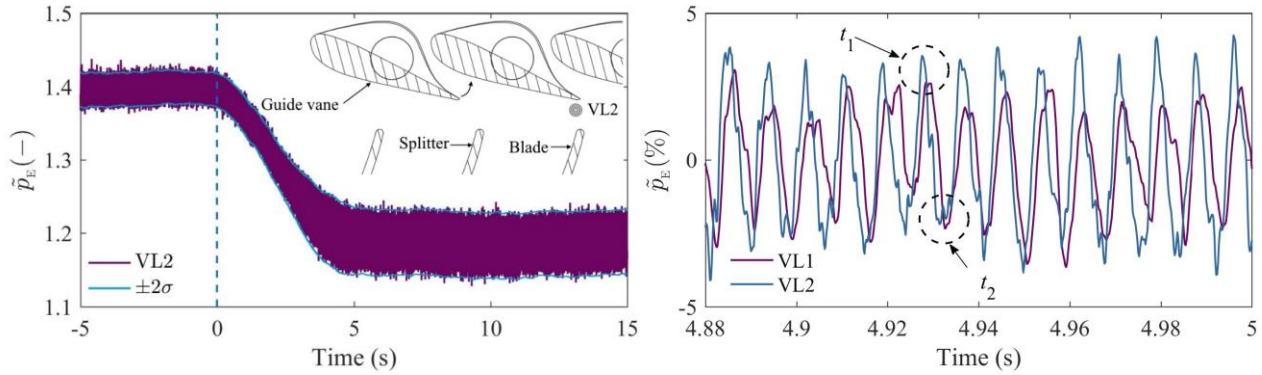

Figure 8 Pressure variation at vaneless space during 30% load reduction. t_1-the pressure sensor is exactly front of a blade. t_2-the sensor is in between a blade and the neighboring splitter. Time 4.88-5 s correspond to ~180° runner rotation.

Spectral analysis was performed to investigate the frequencies and amplitudes in the vaneless space (location VL2). The amplitudes were normalized using Equation (14). Three distinctive frequencies

were obtained. A frequency of runner angular speed (5.5 Hz) and the second harmonic (11 Hz) were observed with approximately 0.1 and 0.09% amplitudes, respectively. A frequency of blade passing (f_b) was observed with the highest amplitudes in the turbine, which were 3% of ρE. Time-domain amplitude variation is shown in Figure 9. Three frequencies, $\frac{f_b}{2}$, f_b, and $2f_b$, are shown. The circle diameter represents the amplitudes. The amplitudes during the load change were small whereas at the end of load change, between 4.5 and 5.5 s, the amplitudes suddenly increased 30-fold. The similar trend was seen for $\frac{f_b}{2}$ and $2f_b$. At steady load, after 7 s, the amplitudes were constant (2.4%). The amplitudes at steady 70% load were 3 times that of the steady BEP load.

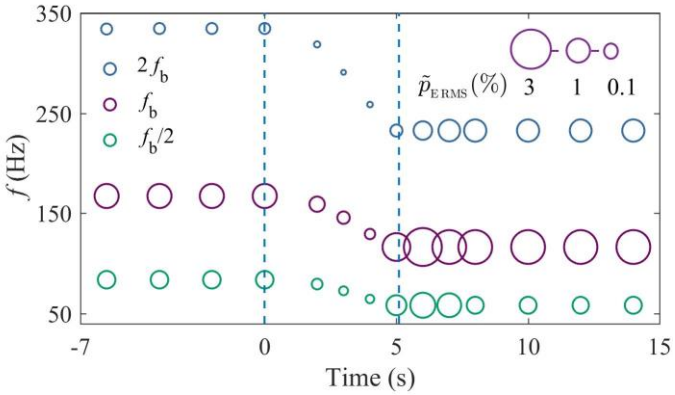

Figure 9 Pressure amplitudes of the blade passing frequency (f_b) and its harmonics in vaneless space (VL2) during load reduction. Time 0 and 5 s corresponds to start and end time of load change, respectively.

Unsteady pressure variation in the runner is shown in Figure 10. Axis scale for both plots is different. Sensor R1 was located 75 mm from the runner inlet edge, and the sensor R4 was located 10 mm before the blade trailing edge. The factor of pressure fluctuations ($\tilde{p}_E$) varies from 1.15 to 0.7 in the runner. As load from BEP reduced, amplitudes of pressure pulsations increased at all locations in the runner. Spectral analysis of the pressure data at R1 location is shown in Figure 10 (right). Amplitudes of guide vane passing frequency (f_{gv}) are shown,

$$f_{gv} = nZ_{gv} \quad \text{(Hz)}. \tag{16}$$

At BEP, the amplitudes are approximately 1%, which decreased to 0.5% during load change. At 70% load (after 4.5 s), the amplitudes increased rapidly up to 2.3%. The second harmonic of f_{gv} was also

obtained with amplitudes of 0.5%. Addition to f_{gv}, frequencies of runner angular speed, second and third harmonics were obtained with small amplitudes (0.1%). Interestingly, f_b was obtained in the runner with amplitudes of 1%. Generally, f_b is observed in the stationary domains such as spiral casing, vaneless space and draft tube. It is rarely observed in the runner. However, spectral analysis at R3 and R4 locations did not show the amplitudes of the f_b.

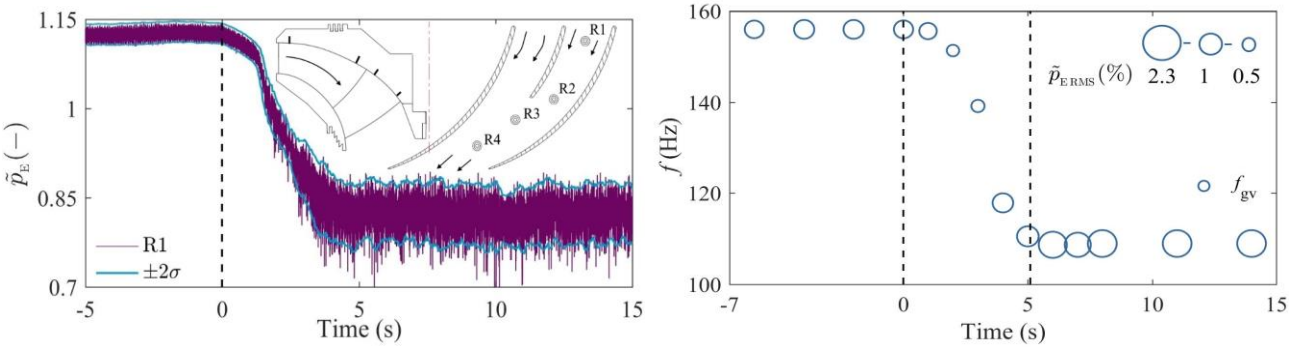

Figure 10 Pressure variation in the runner, locations R1, during load change. Right side plot shows pressure amplitudes of the guide vane passing frequency (f_{gv}). Circle diameter is normalized by the maximum amplitudes of f_{gv}.

Unsteady pressure variation in the draft tube cone is shown in Figure 11. Piezo-electric type four pressure sensors were mounted on the draft tube to extract pressure fluctuations. Thus, sensors showed relative pressure variation from a reference value, i.e. start of load change. During the guide vanes closing period, pressure decreased then slowly recovered. A spectral analysis showed two distinct frequencies, 41.6 Hz and 116. 7 Hz with high amplitudes. The frequency of 41.6 Hz is associated with the standing waves originated from the downstream tank, which was connected to the draft tube outlet. The frequency of 116.7 Hz was related to the blade passing frequency at that load. Peak-to-peak amplitudes of the blade passing frequency were 0.8% of the head. At this load, no frequency of vortex rope was observed. This is due to low runner speed and hence low tangential velocity of the flow leaving the runner. However, when the turbine is operated at the same load but at synchronous speed (5.5 Hz), vortex rope effect is maximum. Another case of load reduction is presented to investigate the time-dependent variation of the vortex rope. In this case, load to the turbine is reduced from PL where the effect of vortex rope is maximum. Figure 12 shows the pressure pulsations associated with the vortex rope frequency (f_{rh}). It can be seen that the vortex rope effect continues up to 6.5 s after the load change.

Figure 12 (right)**Error! Reference source not found.** shows enlarged view of the vortex rope frequency from 4 to 8 s. The frequency of vortex rope is clearly seen, both DT1 and DT2 show 180° out-of-phase variation. After 6.5 s, the only frequency of pressure pulsations is the blade passing frequency in the draft tube. Thus, variable-speed technology can help to improve dynamic stability of the turbine at off-design load.

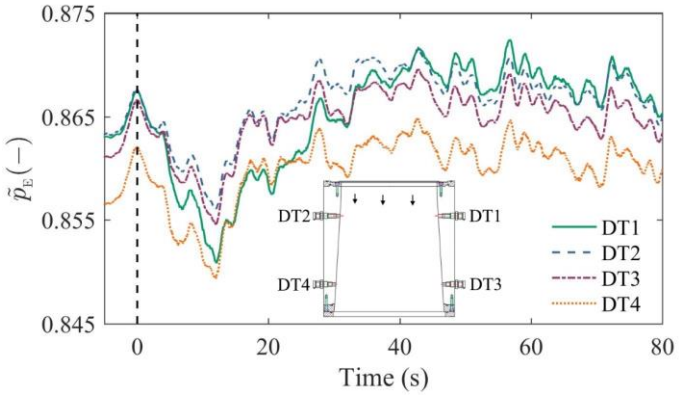

Figure 11 Unsteady pressure variation in the draft tube during load reduction from BEP. Time t=0 s corresponds to start time of load change.

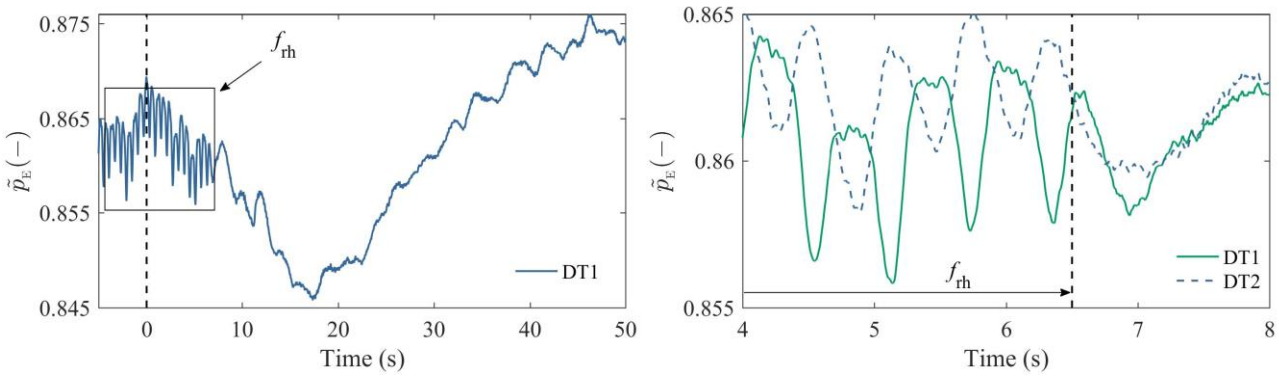

Figure 12 Pressure pulsation of vortex rope frequency (f_{rh}) during load reduction from PL. Dash line at 0 s indicates the start time of load reduction from PL.

3.2 Load acceptance (ramp-up)

Measurements of load acceptance were conducted for the same transient cycles; i.e. increase power output from the previous load reduction point to BEP/PL/FL. In the current section, load acceptance from 40 to 65% load (i.e. PL) is elaborated. Figure 13 shows guide vane angle, runner angular speed, torque and power during load acceptance. Guide vanes and runner angular speed were changed linearly. Turbine was operating at 40% load where the guide vane position and runner angular speed were 40% and 3.9 Hz, respectively. The 65% load was obtained at 5.1 s. Variation of power was quite different

from that of the load reduction case. During load acceptance, power increased linearly whereas torque decreased around 2% initially then increased, after overcoming the mechanical inertia of the rotating structure. The linear increase of power ($T\omega$) during three seconds is due to increase of ω because $P=T\omega$.

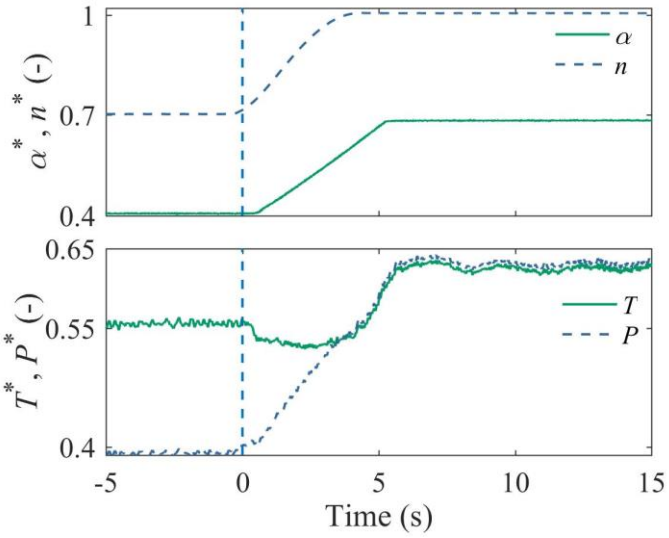

Figure 13 Change of guide vane angle (α), runner angular speed (n), torque (T) and power output (P) during 25% load acceptance. Time t=0 s corresponds to start time of load change.

Two important flow characteristics were observed during analysis of the load reduction data: (1) the maximum amplitudes of RSI frequency from the beginning of PL operating point and (2) strong effect of vortex rope, which gradually dampened as load reduced further. Therefore, it is meaningful to elaborate the load acceptance for the same transient condition, i.e. PL, for more insight. Unsteady pressure variation in the conduit is shown in Figure 14. Pressure is time-averaged over 0.1 s and normalized using Equation (13). The surge oscillations due to guide vanes opening can be seen. Approximately 2% head is dropped initially then recovered. The frequency of oscillations is 1.9 Hz. Similar to the load rejection cases, four distinct frequencies, 15, 27 and 41 Hz were obtained. Further, a frequency of blade passing was obtained before and after the transient, and the respective amplitudes were 0.08 and 0.03%. Unexpectedly, during this load variation, a frequency of guide vane passing was obtained at IN2 location. This is rare occurrence in a hydraulic turbine. However, the amplitudes were small, i.e., 10% of the blade passing frequency. Presence of guide vane passing frequency may be due to the multiplier combinations of stay vanes (14) and guide vanes (28) in the turbine, and the reflection of travelling waves from the spiral casing.

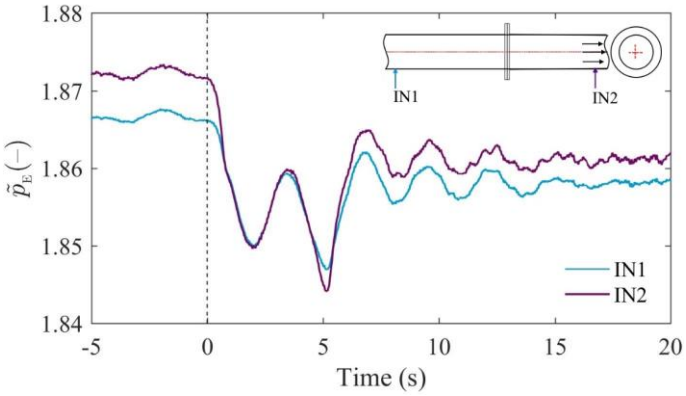

Figure 14 Time-average pressure variation at the turbine inlet conduit during load acceptance from 40% steady load. Dash line at 0 s indicates the start time of load change.

High amplitudes frequencies in the vaneless space were the blade passing and the runner frequencies, including their harmonics. Time-average pressure variation in the vaneless space (locations VL1 and VL2) is shown in Figure 15. The pressure fluctuation factor ($\tilde{p}_E$) varied from 1.2 to 1.4, which was equivalent to 2% head rise. Unsteady pressure amplitudes of the blade passing frequency for two revolutions can be seen in Figure 15 (right)**Error! Reference source not found.**. The pressure amplitudes at 40% and 65% load were 1.3 and 1.2%, respectively. For the second harmonic, the amplitudes were small (<0.1%), which gradually increased to 0.5% at 70% load. More interestingly, amplitudes of vortex rope frequency were observed in the vaneless space when the load was 58% (t=3 s).

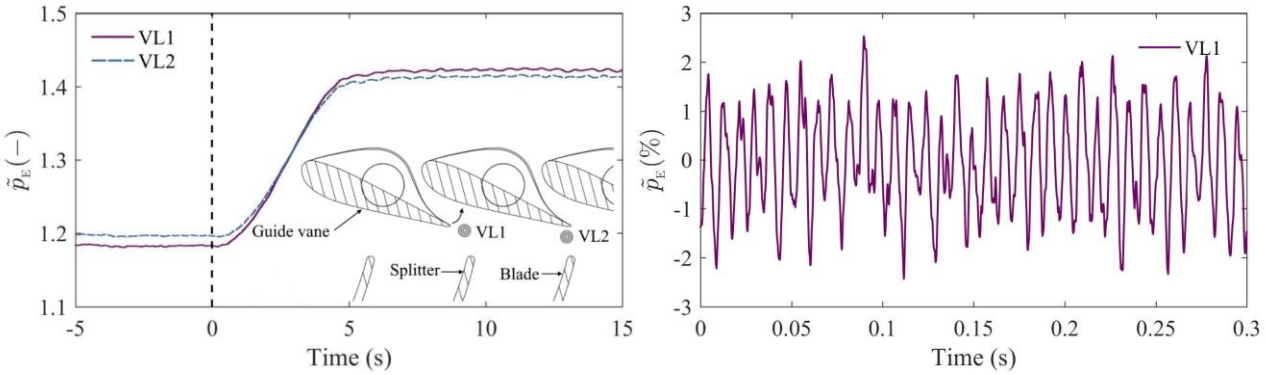

Figure 15 Time-average pressure variation in the vaneless space during load acceptance from 40% steady load. Dash line at 0 s indicates the start time of load change. VL1 and VL2 are locations of the pressure measurement in the vaneless space.

The trend of time-average pressure variation in the runner was similar to that observed for the vaneless space. However, the amplitudes of RSI frequencies were different. Time-average pressure variation at R1, R2, R3 and R4 locations is shown in Figure 16. Pressure loading at R1 location is

maximum, which is approximately 22%, and at other locations is less than 5%. Spectral analysis of the pressure pulsations showed frequencies related to runner angular speed (n), guide vane passing frequency (f_{gv}), blade passing frequency (f_b) and vortex rope (f_{rh}). The maximum amplitudes in the runner corresponded to f_{gv} and the second harmonic. The frequency of runner angular speed and the second harmonic were obtained at all locations in the runner with the amplitudes of 8% of f_{gv}. The amplitudes of f_{gv} are shown in Figure 16 (right)**Error! Reference source not found.**, which are 1% to 0.3% of $(\rho E)_{BEP}$ for R1 to R4, respectively. However, during load change, the amplitudes were small, i.e., less than 0.4% of $(\rho E)_{BEP}$. Similar to the load reduction case, a frequency of blade passing was obtained in the runner. A frequency of vortex rope was obtained at R4 after 4 s as load approached to PL.

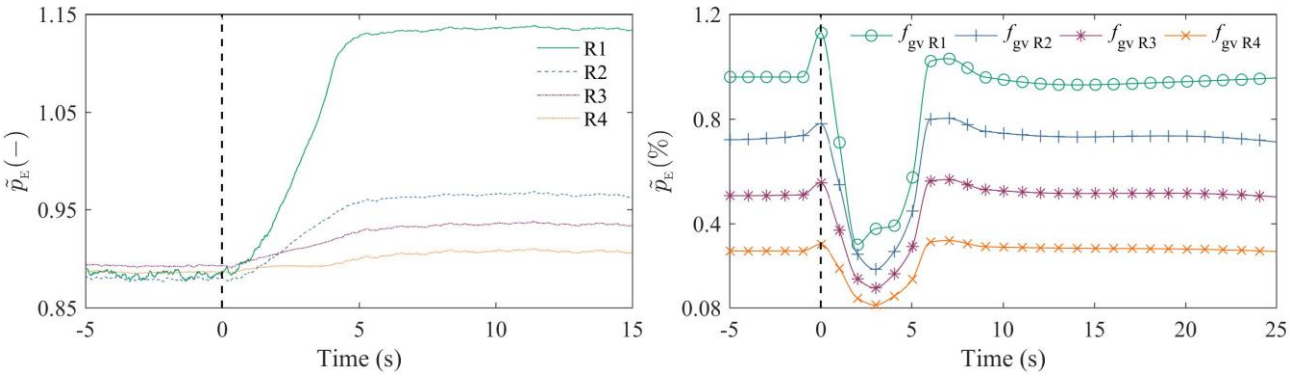

Figure 16 Time-average pressure variation (left) and amplitudes of guide vane passing frequency (right) in the runner loading load acceptance from 40% load. R1, R2, R3 and R4 are the locations pressure measurement starting from runner inlet to the outlet. Time t=0 s corresponds to start time of load change.

Four pressure sensors were mounted to investigate the unsteady pressure pulsations associated with the vortex rope frequency in the turbine. When proper combinations of runner speed and discharge were met, vortex rope began to develop steadily at 4.4 s (see Figure 17). Tangential velocity of the swirling flow was increased with runner angular speed, and same time increase of discharge added momentum. When the load was approximately 58% (at 3 s), vortex rope steadily developed. At DT1 and DT2 locations, amplitudes gradually increase and the phase difference between them is 180°. As load approached to 65%, the f_{rh} was appeared clearly. To investigate the presence of synchronous component (axial), further analysis was carried out. Details about the synchronous and asynchronous components of vortex rope can be found in literature [49–52]. A pressure signal includes a synchronous, an

asynchronous and a random component, i.e., $\tilde{p}_{\mathrm{E}} = \tilde{p}_{\mathrm{E\,syn}} + \tilde{p}_{\mathrm{E\,asyn}} + \tilde{p}_{\mathrm{E\,rand}}$. Both synchronous and asynchronous components can be decomposed as,

$$\tilde{p}_{\mathrm{E\,syn}} = \frac{\tilde{p}_{\mathrm{E\,DT1}} + \tilde{p}_{\mathrm{E\,DT2}}}{2}, \tag{17}$$

$$\tilde{p}_{\mathrm{E\,asyn}} = \frac{\tilde{p}_{\mathrm{E\,DT1}} - \tilde{p}_{\mathrm{E\,DT2}}}{2}. \tag{18}$$

During the transient period, discharge increases constantly hence axial velocity is high as compared to that steady operating condition. At 40% load, the amplitudes are zero as three was no vortex rope. During load change, amplitudes of synchronous component are 0.05% and no asynchronous component. As load approached to 65%, amplitudes of asynchronous component increase rapidly, which are almost six times that of the synchronous components. Thus, effect of rotating vortex rope become stronger than that of the axial, between runner and draft tube elbow.

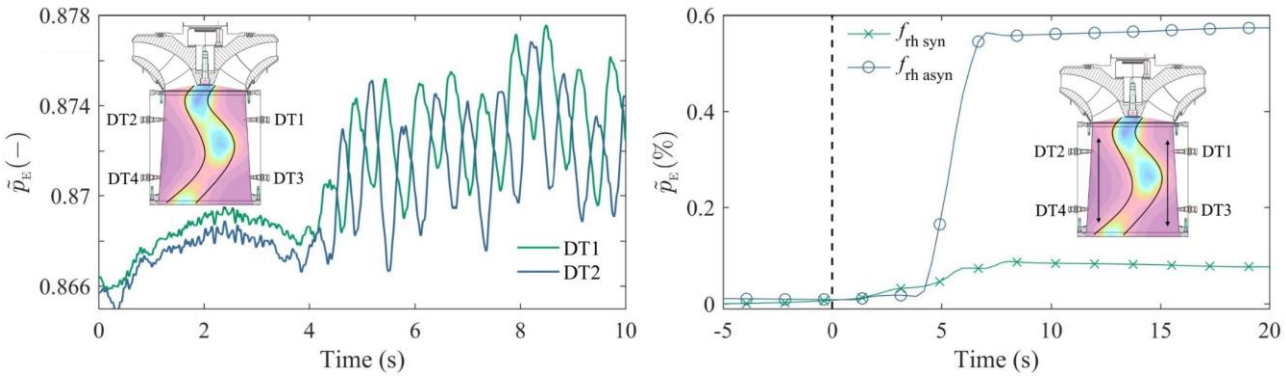

Figure 17 Unsteady pressure variation in the draft tube at DT1 and DT2 locations. Right side plot shows decomposed components of pressure pulsations.

4. Conclusions

Experiments were conducted on a high head Francis turbine during load variation, i.e., load reduction and acceptance. In the previous work [47], we investigated pressure amplitudes by changing rotational speed of the runner only, and the pressure amplitudes were moderate. In the current work, we included variation in discharge as well; both runner angular speed and discharge were changed. Because, inertia of the rotating masses is dependent on the rate of guide vane movement (i.e., instantaneous discharge) and the runner rotational speed, which play key role during steep ramping. For example, load can be

changed instantly by changing the rotational speed where the inertia of rotating masses can help. Mean time hydraulic torque can be changed steadily by opening/closing of guide vanes that allow smooth blade loading and water hammer. However, for a load reduction (steep ramp-down), the inertia can affect adversely. Decrease of runner angular speed (to reduce the load) can increase torque (due to inertia/momentum); consequently, reduction of load may be negligible. The opposite behavior of torque could be associated with the increase of velocity c_{u1}, which resulted in the increase of specific energy until the c_{m1} converged. The findings indicate that well-calibrated approach for the rate of change of runner angular speed, discharge and the inertia (water mass at that load and the rotating structure) is essential while configuring the variable-speed in a turbine.

To investigate the amplitudes of unsteady pressure pulsations, pressure sensors in the vaneless space, runner, draft tube and the conduit were mounted. The results indicated that, during ramping-up or -down, amplitudes of characteristic frequencies such as blade passing and guide vane passing are small. However, at the last phase of ramping, the amplitudes quickly increase, which are up to 30-fold in the vaneless space and runner. We recommend smooth closing/opening of guide vanes during last phase of ramping that will reduce the instant increase of amplitudes. Results from the runner pressure sensors showed presence of blade passing frequency (which is rare occurrence in a high head turbine) during steep ramping. If this is the case for other turbines, to avoid possible conflict and resonance in a turbine, safe distance among, blade passing frequency, guide vane passing frequency and runner natural frequency should be maintained. Spectral analysis in the draft tube during load acceptance showed strong effect of vortex rope, where synchronous type pulsations were dominating for two seconds. Overall, for the variable-speed technology, proper combination of two variables, discharge and runner angular speed, enables safe and dynamically stable operation at off-design unlike synchronous machine. Furthermore, in case of variable-speed operation water hammer and draft tube surging effect is low that allows smooth operation of the turbine and maintains dynamic stability, which big concern for synchronous speed machines.

5. Prospective study

The prospective study will focus on following three objectives:

- Investigate the fatigue loading during load variation. Strain gauges will be mounted on the blades where the compressible/tensile stresses will be measured.
- Investigate the flow field inside the turbine during these transient conditions, particularly vaneless space and blade passages. Numerical study will be carried out where the guide vane will be operated using dynamic mesh technique.
- Investigate the optimum blade loading for the selected transient conditions.

Nomenclatures

BEP	Best efficiency point
DT	Draft tube
FL	Full load
GV	Guide vane
IN	Inlet
OP	Operating point
PL	Part load
RMS	Room mean square
RSI	Rotor stator interaction

c	Flow velocity (m s^{-1})
D	Diameter (m)
E	Specific hydraulic energy (J kg^{-1}); $E=gH$
f	Frequency (Hz)
g	Gravity (m s^{-2}); g = 9.821465 m s^{-2}
H	Head (m)
J	Polar moment of inertia (kg m^{-2})
m	Mass flow rate (kg s^{-1})
n	Runner angular speed (rev s^{-1})
n_{ED}	Speed factor (-)
P	Power (W)
p	Pressure (Pa)
$\tilde{p}_E$	Factor of pressure pulsations (-); $\tilde{p}_E=\tilde{p}/\rho E$
Q	Discharge (m^3 s^{-1})
Q_{ED}	Discharge factor (-)
q	Discharge from labyrinth seals (m^3 s^{-1})
r	Radius (m)
T	Torque (N m)
t	Time (s)
u	Tangential velocity (m s^{-1})
w	Relative velocity (m s^{-1})
Z	Number of blades/guide vanes

Greek letters

η	Efficiency (-)

α Guide vane angle (°)
β Blade angle (°)
ω Angular speed (rad s^{-1}), acceleration (m s^{-2})
δ Uncertainty (%)
ρ water density (kg m^{-3}); ρ=999.8 kg m^{-3}
σ Standard deviation (Pa)

subscript
b Blade
h Hydraulic
m Mean component of a velocity, mechanical
r Random
rh Rheingans frequency/ vortex rope frequency
s Systematic
t Total
u Whirl component of a velocity

Acknowledgement

Investigations are conducted under a research project HydroCen-FME, which is supported by both The Research Council of Norway and industrial partners. One of the objectives is how to reduce the fatigue loading, and find out the way for flexible turbine operation in order to cope with current trend of electricity demand.

References

[1] T. Gjengedal, Integration of wind power and the impact on power system operation, in: IEEE, Montreal, Quebec, Canada, 2003: pp. 76–83. doi:10.1109/LESCPE.2003.1204683.
[2] G. Caralis, D. Papantonis, A. Zervos, The role of pumped storage systems towards the large scale wind integration in the greek power supply system, Renew. Sustain. Energy Rev. 16 (2012) 2558–2565. doi:10.1016/j.rser.2012.01.068.
[3] C. Nicolet, Hydroacoustic modelling and numerical simulation of unsteady operation of hydroelectric systems, Ph. D., Ecole Polytechnique Federale de Lausanne, 2007.
[4] T. Kolšek, J. Duhovnik, A. Bergant, Simulation of unsteady flow and runner rotation during shut-down of an axial water turbine, J. Hydraul. Res. 44 (2006) 129–137. doi:10.1080/00221686.2006.9521668.
[5] M.V. Magnoli, Numerical simulation of pressure oscillations in large Francis turbines at partial and full load operating conditions and their effects on the runner structural behaviour and fatigue life, Ph. D., Technische Universitat Munchen, 2014.
[6] P. Dörfler, M. Sick, A. Coutu, Flow-induced pulsation and vibration in hydroelectric machinery, First, Springer-Verlag, London, England, 2013. http://dx.doi.org/10.1007/978-1-4471-4252-2.
[7] H. Keck, T. Weiss, W. Michler, M. Sick, Recent developments in the dynamic analysis of water turbines, Proc. Inst. Mech. Eng. Part J. Power Energy. 223 (2009) 415–427. doi:10.1243/09576509JPE578.
[8] C. Farell, J. Arroyave, N. Cruz, J. Gulliver, Hydrodynamics of variable speed turbines, University of Minnesota, Minnesota, USA, 1983.

[9] C. Farell, J. Gulliver, Hydromechanics of variable speed turbines, J. Energy Eng. 113 (1987) 1–13. doi:10.1061/(asce)0733-9402(1987)113:1(1).
[10] M. Gagnon, N. Jobidon, M. Lawrence, D. Larouche, Optimization of turbine startup: Some experimental results from a propeller runner, IOP Conf. Ser. Earth Environ. Sci. 22 (2014) 032022. doi:10.1088/1755-1315/22/3/032022.
[11] B.H. Bakken, T. Bjorkvoll, Hydropower unit start-up costs, in: IEEE, Chicago, IL, USA, USA, 2002: pp. 1522–1527. doi:10.1109/PESS.2002.1043646.
[12] H.-J. Huth, Fatigue design of hydraulic turbine runners, Ph. D., Norwegian University of Science and Technology (NTNU), 2005.
[13] C. Trivedi, B. Gandhi, M. Cervantes, Effect of transients on Francis turbine runner life: A review, J. Hydraul. Res. 51 (2013) 121–132. doi:10.1080/00221686.2012.732971.
[14] O. Nilsson, D. Sjelvgren, Hydro unit start-up costs and their impact on the short term scheduling strategies of swedish power producers, IEEE Trans. Power Syst. 12 (1997) 38–44. doi:10.1109/59.574921.
[15] E. Moisan, D.-B. Giacobbi, M. Gagnon, F. Léonard, Self-excitation in Francis runner during load rejection, IOP Conf. Ser. Earth Environ. Sci. 22 (2014) 032025. doi:10.1088/1755-1315/22/3/032025.
[16] L.Y. He, Z.W. Wang, S. Kurosawa, Y. Nakahara, Resonance investigation of pump-turbine during startup process, IOP Conf. Ser. Earth Environ. Sci. 22 (2014) 032024. doi:10.1088/1755-1315/22/3/032024.
[17] U. Seidel, C. Mende, B. Hübner, W. Weber, A. Otto, Dynamic loads in Francis runners and their impact on fatigue life, IOP Conf. Ser. Earth Environ. Sci. 22 (2014) 032054. doi:10.1088/1755-1315/22/3/032054.
[18] B. Hübner, W. Weber, U. Seidel, The role of fluid-structure interaction for safety and life time prediction in hydraulic machinery, IOP Conf. Ser. Earth Environ. Sci. 49 (2016) 072007. doi:10.1088/1755-1315/49/7/072007.
[19] C. Mende, W. Weber, U. Seidel, Progress in load prediction for speed-no-load operation in Francis turbines, IOP Conf. Ser. Earth Environ. Sci. 49 (2016) 062017. doi:10.1088/1755-1315/49/6/062017.
[20] B. Nennemann, J.F. Morissette, J. Chamberland-Lauzon, C. Monette, O. Braun, M. Melot, A. Coutu, J. Nicolle, A.M. Giroux, Challenges in dynamic pressure and stress predictions at no-load operation in hydraulic turbines, IOP Conf. Ser. Earth Environ. Sci. 22 (2014) 032055. doi:10.1088/1755-1315/22/3/032055.
[21] J. Morissette, J. Chamberland-Lauzon, B. Nennemann, C. Monette, A. Giroux, A. Coutu, J. Nicolle, Stress predictions in a Francis turbine at no-load operating regime, IOP Conf. Ser. Earth Environ. Sci. 49 (2016) 072016. doi:10.1088/1755-1315/49/7/072016.
[22] C. Monette, H. Marmont, J. Chamberland-Lauzon, A. Skagerstrand, A. Coutu, J. Carlevi, Cost of enlarged operating zone for an existing Francis runner, IOP Conf. Ser. Earth Environ. Sci. 49 (2016) 072018. doi:10.1088/1755-1315/49/7/072018.
[23] J. Nicolle, A.M. Giroux, J.F. Morissette, CFD configurations for hydraulic turbine startup, IOP Conf. Ser. Earth Environ. Sci. 22 (2014) 032021. doi:10.1088/1755-1315/22/3/032021.
[24] C. Trivedi, M.J. Cervantes, Fluid structure interaction in hydraulic turbines: a perspective review, Renew. Sustain. Energy Rev. 68 (2017) 87–101. doi:10.1016/j.rser.2016.09.121.
[25] C. Trivedi, A review on fluid structure interaction in hydraulic turbines: A focus on hydrodynamic damping, Eng. Fail. Anal. 77 (2017) 1–22. doi:10.1016/j.engfailanal.2017.02.021.
[26] W. Zeng, J. Yang, J. Hu, J. Yang, Guide-vane closing schemes for pump-turbines based on transient characteristics in S-shaped region, J. Fluids Eng. 138 (2016) 051302. doi:10.1115/1.4032069.
[27] K. Amiri, B. Mulu, M. Raisee, M.J. Cervantes, Unsteady pressure measurements on the runner of a Kaplan turbine during load acceptance and load rejection, J. Hydraul. Res. 54 (2016) 56–73. doi:10.1080/00221686.2015.1110626.

[28] C. Trivedi, M. Cervantes, B. Gandhi, O. Dahlhaug, Experimental investigations of transient pressure variations in a high head model Francis turbine during start-up and shutdown, J. Hydrodyn. Ser B. 26 (2014) 277–290. doi:10.1016/S1001-6058(14)60031-7.
[29] C. Trivedi, M. Cervantes, B. Gandhi, O. Dahlhaug, Pressure measurements on a high-head Francis turbine during load acceptance and rejection, J. Hydraul. Res. 52 (2014) 283–297. doi:10.1080/00221686.2013.854846.
[30] C. Trivedi, M. Cervantes, O. Dahlhaug, B. Gandhi, Experimental investigation of a high head Francis turbine during spin-no-load operation, J. Fluids Eng. 137 (2015) 061106. doi:10.1115/1.4029729.
[31] C. Trivedi, B. Gandhi, M. Cervantes, O. Dahlhaug, Experimental investigations of a model Francis turbine during shutdown at synchronous speed, Renew. Energy. 83 (2015) 828–836. doi:10.1016/j.renene.2015.05.026.
[32] C. Trivedi, M. Cervantes, B. Gandhi, O. Dahlhaug, Transient pressure measurements on a high head model Francis turbine during emergency shutdown, total load rejection, and runaway, J. Fluids Eng. 136 (2014) 121107. doi:10.1115/1.4027794.
[33] C. Trivedi, M.J. Cervantes, B.K. Gandhi, Numerical investigation and validation of a Francis turbine at runaway operating conditions, Energies. 9 (2016) 22. doi:10.3390/en9030149.
[34] Z. Zuo, S. Liu, Y. Sun, Y. Wu, Pressure fluctuations in the vaneless space of high-head pump-turbines-a review, Renew. Sustain. Energy Rev. 41 (2015) 965–974. doi:10.1016/j.rser.2014.09.011.
[35] X. Liu, Y. Luo, Z. Wang, A review on fatigue damage mechanism in hydro turbines, Renew. Sustain. Energy Rev. 54 (2016) 1–14. doi:10.1016/j.rser.2015.09.025.
[36] C. Widmer, T. Staubli, N. Ledergerber, Unstable characteristics and rotating stall in turbine brake operation of pump-turbines, J. Fluids Eng. 133 (2011) 041101. doi:10.1115/1.4003874.
[37] S. Pejovic, B. Karney, Guidelines for transients are in need of revision, IOP Conf. Ser. Earth Environ. Sci. 22 (2014) 042006. doi:10.1088/1755-1315/22/4/042006.
[38] M. Gagnon, J. Nicolle, J.F. Morissette, M. Lawrence, A look at Francis runner blades response during transients, IOP Conf. Ser. Earth Environ. Sci. 49 (2016) 052005. doi:10.1088/1755-1315/49/5/052005.
[39] C. Trivedi, M.J. Cervantes, O.G. Dahlhaug, Numerical techniques applied to hydraulic turbines: A perspective review, Appl. Mech. Rev. 68 (2016) 010802. doi:10.1115/1.4032681.
[40] J. Nicolle, J. Morissette, A. Giroux, Transient CFD simulation of a Francis turbine startup, IOP Conf. Ser. Earth Environ. Sci. 15 (2012) 062014. doi:10.1088/1755-1315/15/6/062014.
[41] H. Hosseinimanesh, C. Devals, B. Nennemann, M. Reggio, F. Guibault, A numerical study of Francis turbine operation at no-load condition, J. Fluids Eng. 139 (2016) 011104. doi:10.1115/1.4034422.
[42] C. Trivedi, Investigations of compressible turbulent flow in a high head Francis turbine, J. Fluids Eng. 140 (2018) 011101. doi:10.1115/1.4037500.
[43] F. Dompierre, M. Sabourin, Determination of turbine runner dynamic behaviour under operating condition by a two-way staggered fluid-structureinteraction method, IOP Conf. Ser. Earth Environ. Sci. 12 (2010) 012085. doi:10.1088/1755-1315/12/1/012085.
[44] H. Schmucker, F. Flemming, S. Coulson, Two-way coupled fluid structure interaction simulation of a propeller turbine, Int. J. Fluid Mach. Syst. 3 (2010) 342–351. doi:10.5293/IJFMS.2010.3.4.342.
[45] F.-K. Benra, H.J. Dohmen, J. Pei, S. Schuster, B. Wan, A comparison of one-way and two-way coupling methods for numerical analysis of fluid-structure interactions, J. Appl. Math. 2011 (2011) 1–16. doi:10.1155/2011/853560.
[46] P. Mossinger, A. Jung, Transient two-phase CFD simulation of overload operating conditions and load rejection in a prototype sized Francis turbine, IOP Conf. Ser. Earth Environ. Sci. 49 (2016) 092003. doi:10.1088/1755-1315/49/9/092003.

[47] C. Trivedi, E. Agnalt, O.G. Dahlhaug, Investigations of unsteady pressure loading in a Francis turbine during variable-speed operation, Renew. Energy. 113 (2017) 397–410. doi:10.1016/j.renene.2017.06.005.
[48] IEC 60193, Hydraulic turbines, storage pumps and pump-turbines: Model acceptance tests, International Electrotechnical Commission, 3, rue de Varembé, PO Box 131, CH-1211 Geneva 20, Switzerland. 16 November, 1999.
[49] A.I. Bosioc, R. Susan-Resiga, S. Muntean, C. Tanasa, Unsteady pressure analysis of a swirling flow with vortex rope and axial water injection in a discharge cone, J. Fluids Eng. 134 (2012) 081104. doi:10.1115/1.4007074.
[50] P. Doerfler, N. Ruchonnet, A statistical method for draft tube pressure pulsation analysis, IOP Conf. Ser. Earth Environ. Sci. 15 (2012) 062002. doi:10.1088/1755-1315/15/6/062002.
[51] G.K. Rajan, J.M. Cimbala, Computational and Theoretical Analyses of the Precessing Vortex Rope in a Simplified Draft Tube of a Scaled Model of a Francis Turbine, J. Fluids Eng. 139 (2017) 021102. doi:10.1115/1.4034693.
[52] R. Goyal, M.J. Cervantes, B.K. Gandhi, Vortex rope formation in a high head model Francis turbine, J. Fluids Eng. 139 (2017) 041102. doi:10.1115/1.4035224.